Chem

CellPress

Article

Scalable and Sustainable Approach toward Highly Compressible, Anisotropic, Lamellar Carbon Sponge

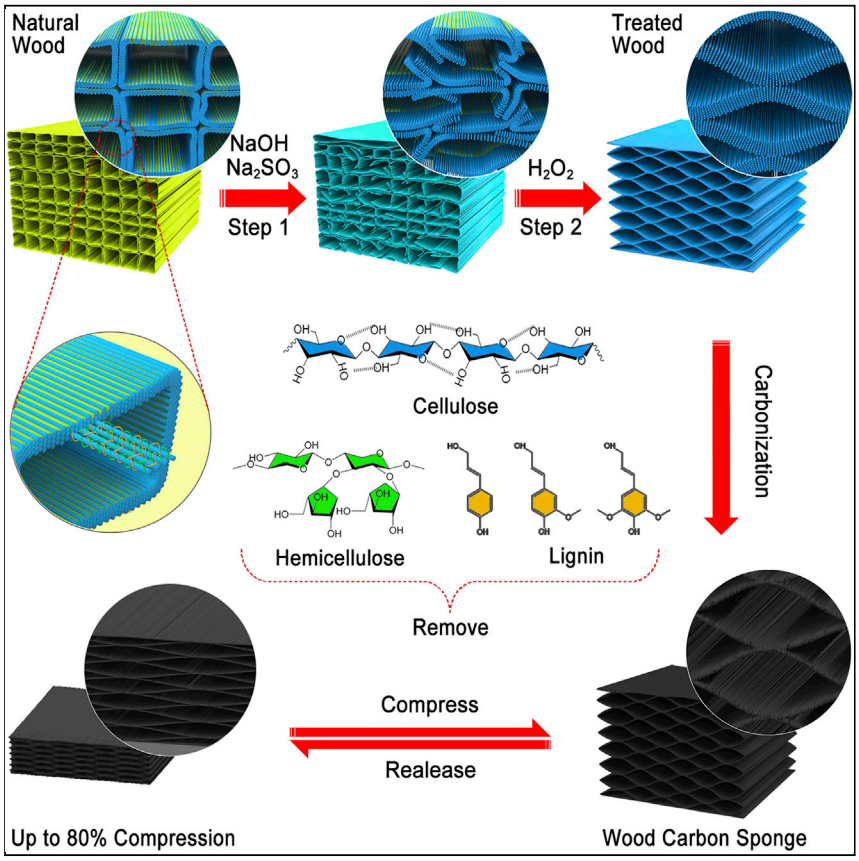

A direct wood-to-carbon-sponge transformation is realized via a facile chemical treatment and subsequent carbonization process. Removing the lignin and hemicellulose from balsa wood cell walls is a significant step toward converting the lattice-like wood structure to a spring-like lamellar structure. Magic transformation from brittle wood carbon to compressible wood carbon sponge thus becomes achievable. The wood carbon sponge exhibits a sensitive electrical response as a strain sensor and attractive features for other potential applications.

Chaoji Chen, Jianwei Song, Shuze Zhu, ..., Teng Li, Jia Xie, Liangbing Hu

lit@umd.edu (T.L.)
xiejia@hust.edu.cn (J.X.)
binghu@umd.edu (L.H.)

HIGHLIGHTS

Direct conversion from natural wood to compressible carbon sponge is realized

The spring-inspired lamellar structure design renders high compressibility

A sensitive electrical response upon pressure can be achieved

Chen et al., Chem 4, 544–554
March 8, 2018 Published by Elsevier Inc.
https://doi.org/10.1016/j.chempr.2017.12.028

Chem

CellPress

Article

Scalable and Sustainable Approach toward Highly Compressible, Anisotropic, Lamellar Carbon Sponge

Chaoji Chen,[1,2,4] Jianwei Song,[1,4] Shuze Zhu,[3,4] Yiju Li,[1] Yudi Kuang,[1] Jiayu Wan,[1] Dylan Kirsch,[1] Lisha Xu,[1] Yanbin Wang,[1] Tingting Gao,[1] Yilin Wang,[1] Hao Huang,[3] Wentao Gan,[1] Amy Gong,[1] Teng Li,[3,*] Jia Xie,[2,*] and Liangbing Hu[1,5,*]

SUMMARY

Here, we demonstrate that wood can be directly converted into a highly compressible wood carbon sponge (WCS) by lignin and hemicellulose removal followed by carbonization. The significant removal of lignin and hemicellulose via chemical treatment destroys the thin cell walls of natural wood, giving rise to a lamellar structure with numerous stacked arched layers. The lamellar structure can be well preserved even after high-temperature carbonization. Interestingly, such a lamellar structure renders a high compressibility up to 80% and high fatigue resistance of 10,000 compression cycles at 50% strain. Further experimental and modeling studies reveal that WCS can accommodate substantial compression from the bending and flattening of the curved layers, resulting in minimum stretching of individual layers. The WCS also demonstrates a sensitive electrical conductivity change upon compression. Using this lamellar sponged structure and the excellent mechanical and electrical properties of WCS as an example, we demonstrate the great potential of WCS for highly sensitive strain sensors.

INTRODUCTION

Lightweight and compressible carbonaceous materials with high conductivity, large surface area, and high porosity can be implemented in various applications such as energy storage, pollutant treatment, electronic devices, and sensors.[1–6] In the past few decades, compressible carbonaceous materials have been constructed from graphene,[2,3,7–9] carbon nanotubes,[10–13] carbon nanofibers,[14] and fullerenes;[15] graphene has been one of the most popular constituents as a result of its excellent electrical and mechanical properties.[16–18] Although these materials demonstrate desirable electrical and mechanical properties, the fabrication process remains complicated, and the starting raw materials usually involve fossil resources that are not renewable. Biomass-based materials, on the other hand, are renewable and more abundant, offering a simple yet attractive alternative approach to construct compressible carbonaceous materials without using the limited fossil resources. On the basis of this concept, several biomass materials such as chitin,[19] bacterial cellulose,[4,20,21] watermelon,[22] and winter melon[23] have been converted into compressible carbonaceous materials recently. However, because of the difficulty with the structural design when using these biomasses, the resulting materials demonstrate inferior electrical and mechanical properties in comparison with those derived from graphene or carbon nanotubes. In addition, most of these approaches are bottom-up methods that involve multiple steps and environment-unfriendly

The Bigger Picture

Lightweight compressible materials enable various applications but are often hindered by limited and unrenewable resources, complex and scale-limited fabrication, and poor mechanical properties. We developed a wood-to-carbon-sponge strategy for fabricating highly lightweight and compressible wood carbon sponge directly from natural balsa wood via a scalable and sustainable top-down approach. The chemical treatment removes lignin and hemicellulose from the wood cell walls, directly converting the lattice-like rigid wood structure into a spring-like compressible lamellar structure. The wood carbon sponge shows outstanding mechanical properties and sensitive electrical responses as a strain sensor. Future applications, including flexible electronics, rechargeable batteries, and catalyst supports, can be expected. Our top-down fabrication strategy opens up new opportunities for developing sponge-like functional materials from sustainable natural resources.

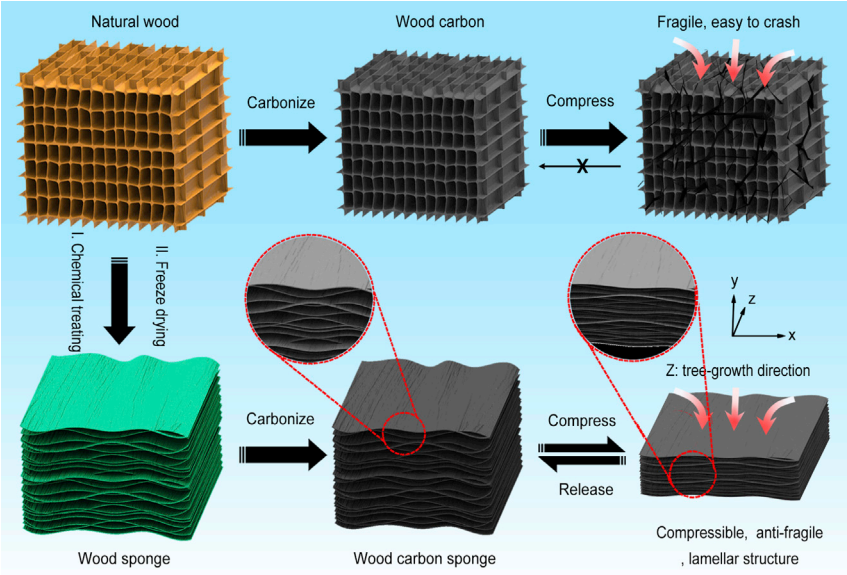

Figure 1. Graphical Illustration of the Design and Fabrication Process of the Fragile WC and the Highly Compressible WCS

As a result of the unique arched layered structure, the WCS has anisotropic mechanical properties and is highly compressible.

chemicals, which may hinder their large-scale application in terms of manufacture efficiency, cost, and scalability. Therefore, it is highly challenging yet desirable to construct compressible carbonaceous materials with good electrical and mechanical properties from renewable biomass materials via a rational structure design in a simple, low-cost, "green," and scalable way.

In terms of a structure design that allows for high mechanical compressibility, examples from daily life give valuable inspiration. One prototypical example is the helical spring that is widely used for shock absorption in various kinds of machines. A spring can accommodate large compression by bending and twisting its helical wire, whereas the stretching in the wire is negligible. As a result, the spring is elastically compressible.[24] One elegant example comes from Yu's group, who constructed a hierarchical spring-like architecture composed of parallel flat lamellas with long-range alignment from chitosan and graphene oxide via a bidirectional freezing process and subsequent annealing.[25] Another highly compressible structure is honeycomb, which comprises a network of wavy layers that can accommodate compression in various directions by flexing and straightening the wavy layers with minimum stretching of the layers.

With inspiration from these examples, we developed a lightweight and highly compressible carbonaceous material, termed wood carbon sponge (WCS), which has a lamellar microstructure with numerous interconnected arch-shaped substructures. The wood-to-carbon-sponge design concept and straightforward top-down fabrication process of the WCS are illustrated in Figure 1. We chose balsa wood (one of the lightest woods) as the starting material because of its unique microstructure, low density, and thin cell wall, which make it easier to partially destroy the cell walls.[26,27] It is commonly known that wood carbon directly carbonized from natural wood is fragile and easily crushed under a certain pressure. Through a simple treatment of lignin and hemicellulose removal followed by carbonization, however, the

[1]Department of Materials Science and Engineering, University of Maryland, College Park, MD 20742, USA

[2]State Key Laboratory of Advanced Electromagnetic Engineering and Technology, School of Electrical and Electronic Engineering, Huazhong University of Science and Technology, Wuhan 430074, P.R. China

[3]Department of Mechanical Engineering, University of Maryland, College Park, MD 20742, USA

[4]These authors contributed equally

[5]Lead Contact

*Correspondence: lit@umd.edu (T.L.), xiejia@hust.edu.cn (J.X.), binghu@umd.edu (L.H.)

https://doi.org/10.1016/j.chempr.2017.12.028

resulting WCS becomes compressible. As a result of this lamellar structure, the treated wood has remarkable mechanical compressibility. The carbonization step does not change the lamellar structure, resulting in WCS material with a unique lamellar structure and excellent mechanical compressibility.

RESULTS AND DISCUSSION

Chemical Treatment of Natural Wood

Chemical treatments play a key role in achieving the unique lamellar structure, as a result of the removal of hemicellulose and lignin in wood structures. As graphically illustrated in Figure 2A, the chemical treatment led to both chemical and structural changes to the balsa wood. Nucleophilic sulfite (SO_3^{2-}) enables the sulfonation of lignin, leading to the removal of lignin. Meanwhile, hemicellulose and partial cellulose can also be dissolved by an alkaline solution containing sulfite. As this process continues, the thin cell walls become porous, and even broken, whereas the thick rays can survive (step 1). Further chemical treatment with H_2O_2 continuously removes lignin and hemicellulose, leading to total breakage of the thin cell walls (step 2). These broken thin cell walls tend to attach onto the nearest unbroken ray under templating of ice during freeze drying, resulting in a unique lamellar structure with multiple stacked and connecting arched layers.

To validate this, we carried out Fourier-transform infrared spectroscopy (FTIR) and compositional analysis of the wood samples before and after chemical treatment. The FTIR spectra of the natural wood and treated wood show that the groups assigned to lignin and hemicellulose were significantly reduced by the mixed solution of NaOH/Na_2SO_3 and H_2O_2 (Figure 2B). Meanwhile, the color of the wood samples changed from yellow to totally white (Figure S1), and the weight changed from 100% to 21% (Figure S2), also indicating the removal of the lignin and hemicellulose components. This can be further confirmed by the compositional analysis, showing that almost all the hemicellulose and lignin components were removed by the chemical treatment (Figure 2C). By removing the lignin and hemicellulose components, the structure of the wood blocks transforms significantly from a latticed structure, comprising numerous lattice-shaped subunits (Figures 2D, 2F, and S3), into a lamellar structure with an array of arch-shaped layers stacked over each other (Figures 2H, 2J, and S4). More magnified scanning electron microscopy (SEM) images show that the cellulose assembly in the individual layer becomes porous as a result of the removal of the hemicellulose and lignin fillers, whereas the alignments of these cellulose nanofibers remain almost the same (Figures 2E, 2G, 2I, and 2K).

Structural Characterization of the Wood Carbon Sponge

Interestingly, the lamellar structure can be well preserved even after high-temperature (1,000°C) carbonization, which can be confirmed by SEM characterization. As shown in Figures 3A–3C, the wood carbon (WC) obtained from carbonizing the natural wood directly inherits the latticed structure of the natural wood, including lattice-like channels of 20–30 μm in size and very thin channel walls of ~1 μm. The WCS material demonstrates a completely different structure in contrast to WC but is similar to that of the wood sponge, with a lamellar structure composed of numerous arch-shaped layers stacked together (top view SEM image; Figures 3D and 3E). The cross-sectional SEM image in Figure 3F shows that the channel walls (cell walls) in the WCS have almost disappeared, resulting in an arch-shaped layered microstructure rather than a lattice-shaped channel. Transmission electron microscopy and Raman results further reveal that WCS has an amorphous nature, which is commonly observed in biomass-derived carbonaceous materials (Figures S5 and S6).[28–33] Because the unique lamellar multi-arched structure contains abundant

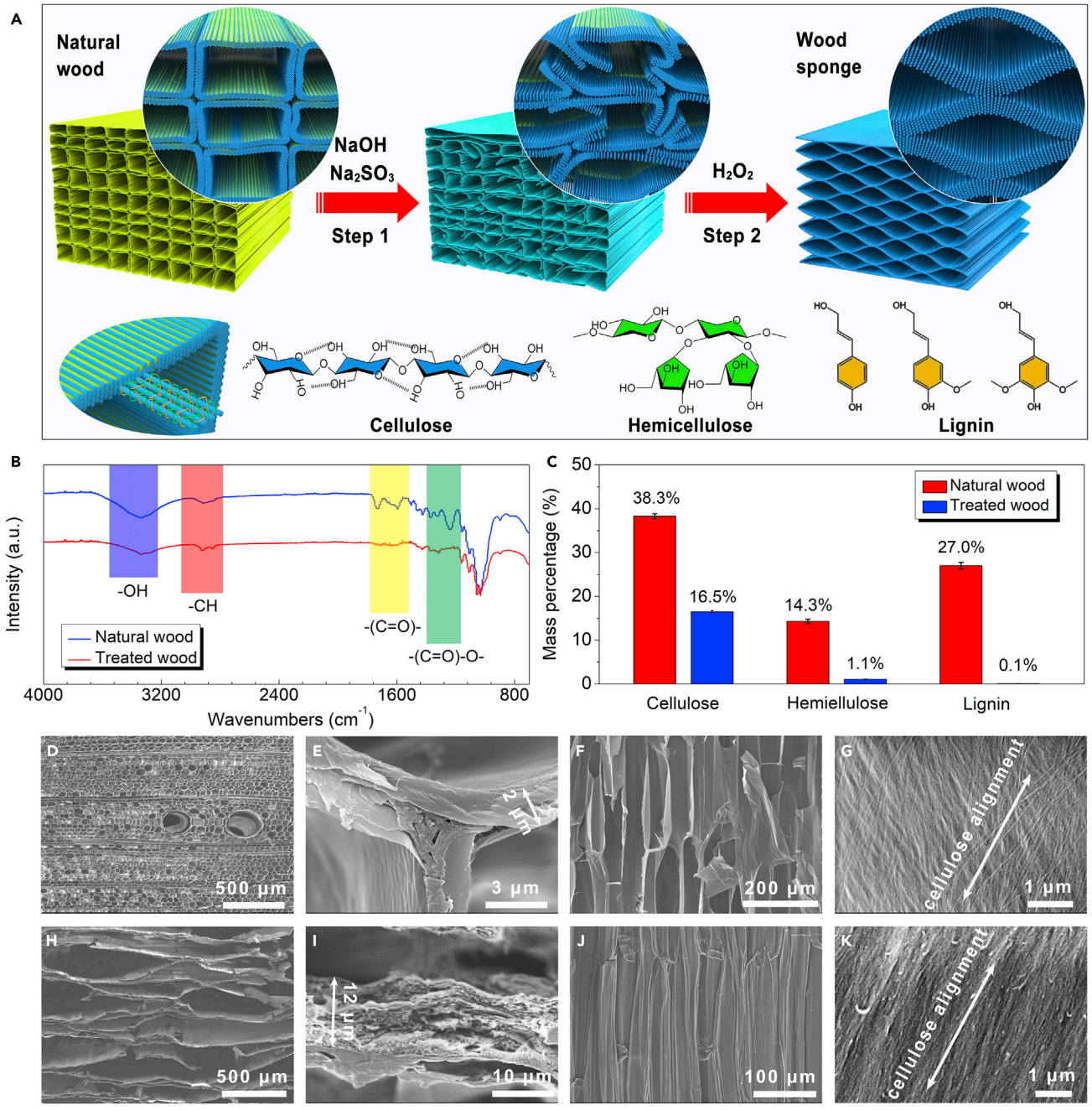

Figure 2. Chemicals and Structure Evolutions of Natural Balsa Wood upon Chemical Treatment

(A) Graphical illustration of the chemicals and structure evolutions of natural balsa wood upon chemical treatment.

(B and C) Composition evolutions of the uncarbonized precursors upon chemical treatment: (B) FTIR spectra and (C) content evolutions of cellulose, hemicellulose, and lignin. Error bars indicate standard deviations for three sets of data points.

(D–G) SEM images of natural wood: (D and E) top view images showing the lattice-like porous structure and (F and G) cross-sectional images showing the open channels (lumina) and the cellulose nanofibers.

(H–K) SEM images of the treated wood (wood sponge): (H and I) top view images showing the lamellar structure with multiple stacked layers and (J and K) in-plane image of an individual layer and the cellulose nanofibers.

pores between each layer, the WCS is highly lightweight with a density of 15 mg cm^{-3}, which is ~10 times lower than the initial untreated natural wood and ~3.5 times lower than the sponge-like delignified wood (Figure S7). Figures

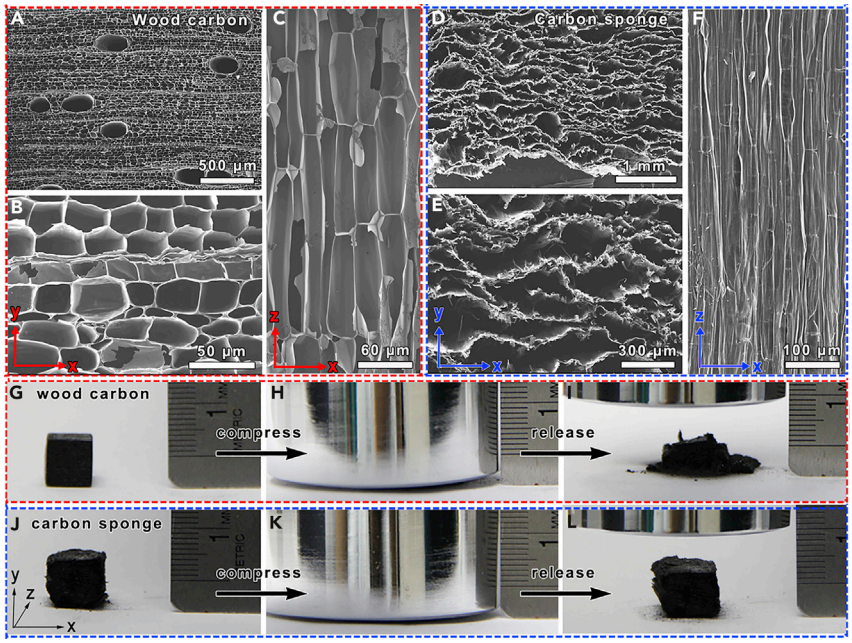

Figure 3. Morphology and Structure Characterization of WC and WCS

(A–C) SEM images of WC directly carbonized from natural wood: (A) top view image from the growth direction, (B) magnified image of (A), and (C) cross-sectional view showing the multiple cell-like channels.

(D–F) SEM images of WCS carbonized from treated wood (wood sponge): (D) top view image from the growth direction, (E) magnified image of (D), and (F) cross-section view showing the multiple lamellar-like channels.

(G–I) Photographs of the WC block before compression (G), under compression (H), and after release (I).

(J–L) Photographs of the WCS block before compression (J), under compression (K), and after release (L).

3G–3L demonstrate the mechanical compressibility of the two distinct carbonaceous materials. Both types of carbonaceous blocks can be compressed by >80% as a result of their high porosity. However, the WC block is highly fragile and deforms permanently (collapsed into small pieces) when compressed by >80% (Figures 3G–3I). Strikingly, the WCS block totally recovers to its original shape without mechanical failure under the same compression (Figures 3J–3L), demonstrating excellent mechanical compressibility.

Mechanical Compressibility and Fatigue Resistance of the Wood Carbon Sponge

To further assess the mechanical properties of the WCS block, we carried out multiple compression tests to measure the compressive stress (σ) as a function of strain (ε). Figure 4A shows the σ-ε plots with different compressive forces, demonstrating three distinct regions during the loading process. The σ-ε plots show a linear stage at $\varepsilon < 20\%$, indicating an elastic modulus that records the elastic bending of the cell walls. As the strain keeps increasing, a plateau stage at $20\% < \varepsilon < 60\%$ emerges, which reflects bending as a result of buckling of the cell walls. When the strain goes above 60%, a non-linear stage with sharply increasing σ appears, suggesting increasing acceleration of the stress requirement to compress the material. The resulting compressive stress-strain behavior is similar to other form-like materials reported previously.[3,4,25,34–38] The maximum ε can be as high as 80% under a σ of 70 kPa, suggesting high compressibility of the WCS. Cyclic compression results

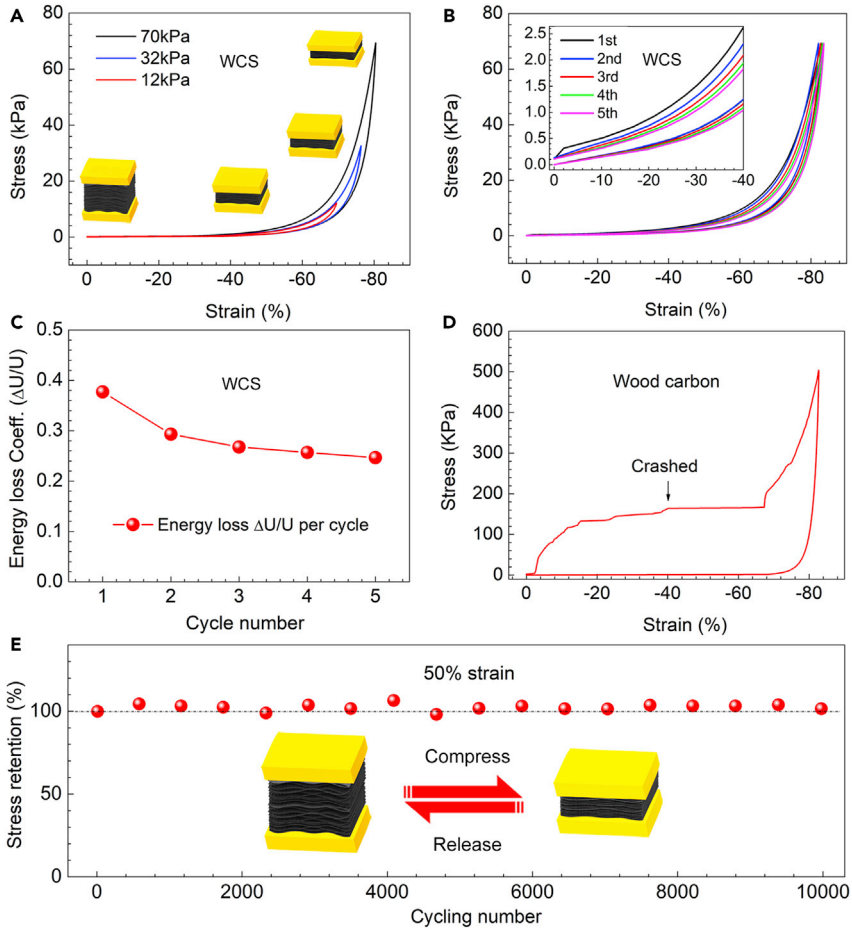

Figure 4. Mechanical Properties of WCS and WC

(A) Stress-strain curves of WCS with different force loadings; insets illustrate the WCS material at different points during compression.

(B) Stress-strain curves of WCS obtained from five repeated cycles.

(C) Energy loss $\Delta U/U$ of WCS during each cycle.

(D) Stress-strain curves of WC.

(E) Elastic strength retention during 10,000 cycles at 50% strain; the inset illustrates the repeated compression of the WCS material.

show small plastic deformation in the initial two cycles, which quickly decreases to nearly zero in the following cycles, indicating the excellent structure stability of WCS (Figure 4B). This can be further confirmed by the energy dissipation of different cycles. As shown in Figure 4C, the energy loss decreases from 0.37 on the first cycle to 0.25 on the fifth cycle, which is much smaller than those of many sponge-like carbonaceous materials reported previously.[39–43] In contrast, the WC block with a latticed structure shows much inferior mechanical compressibility. As demonstrated in Figure 4D, the WC block becomes crushed when ε increases to 40%, suggesting the brittle nature of the WC material. The WCS material is highly stable even after undergoing 10,000 compressing and releasing cycles at a constant strain of 50%, with negligible plastic deformation, suggesting an outstanding fatigue resistance (Figures 4E and S8).

The anisotropic structure of the WCS may lead to anisotropic mechanical properties. To validate this, we further compressed the WCS along the *z* direction (parallel to the

stacked layer). The results show that the WCS can be easily crushed as a result of the relatively weak connection between the layers (Figures S9C and S9D), which is quite distinct from the high compressibility when the stress is applied along the *y* direction (vertical to the stacked layers; Figures S9A and S9B). The distinct compressive properties of the wood carbon sponge along *y* and *z* directions indicate that the WCS has a unique anisotropic mechanical property that is highly related to its anisotropic structure directly derived from balsa. With other kinds of wood, for example, basswood, it is difficult to get such a unique lamellar structure and high compressibility even with the same chemical delignification and freeze-drying treatment process (Figures S10 and S11).

Insights into the Mechanical Compressibility of the Wood Carbon Sponge

To obtain further insight into the compressibility of the WCS, we carried out *ex situ* SEM observations and finite element simulations. The *ex situ* SEM images are presented in Figures S12A–S12D, where the stacked wavy layers of the WCS become straight, and the pore size between the layers decreases significantly under compression. More remarkably, during the compression process, no obvious fracture in the wavy layers is observed even with a high compressive deformation of 80% strain, indicating the excellent compressibility of the WCS material (Figures S12C and S12D). When the compression is released, the straightened layers can completely recover their original wavy shape, further demonstrating the excellent compressibility of the WCS material (Figures S12E and S12F). In contrast, the lattice-structured WC can be easily damaged by compression (Figure S13). The crushing action mainly takes place in the joints of the crossing cell walls, because of the concentration of stress in the joints.

Further finite element simulations (see Supplemental Experimental Procedures and Figure S14 for modeling details) were performed to shed light on the effect of the structural features on the concentration of stress under similar compression loadings for both WCS and WC. The modeling results clearly confirm our hypothesis that the WCS is much more resistant to failure than the untreated WC when subject to compression. Figures 5A and 5B show the mesh-like and wave-like finite element models for WC and WCS, respectively. The difference between the structure of WC and WCS is clearly presented in these two models. The WCS structure is layered. These layers are curved, and as a result, one layer can have contact with the other layer through a localized region on the curved surface, thus alleviating stress. On the other hand, the WC exhibits a more porous structure with many channels. Figures 5C and 5D show the distribution of the Mises stress in both structures when a nominal compression strain of 0.36 is applied, respectively. It is found that the WC structure suffers from much higher stress concentration than the WCS structure, especially at the channel walls running parallel to the compressing direction. By contrast, the WCS structure can accommodate the applied compression by bending its curved layers, leading to a much lower stress. Figure 5E compares the normalized maximum Mises stress in the two structures as a function of the applied nominal compressive strain. It is evident that the maximum stress level in the WCS model is more than four times lower than that in the WC structure. As a result, the WC sample would fail at a much lower load; WCS can sustain a higher load and remain elastic.

Application of the Wood Carbon Sponge as a Strain Sensor

The WCS material also shows a high pressure-resistance sensitivity, which can potentially allow use in a range of applications such as strain sensors, conductivity-tunable conductors, and health monitors. As demonstrated in Figures 6A and 6B, a pressure sensor is made by clamping a WCS slice of 1 cm × 0.5 cm × 1 mm between two pieces of Cu

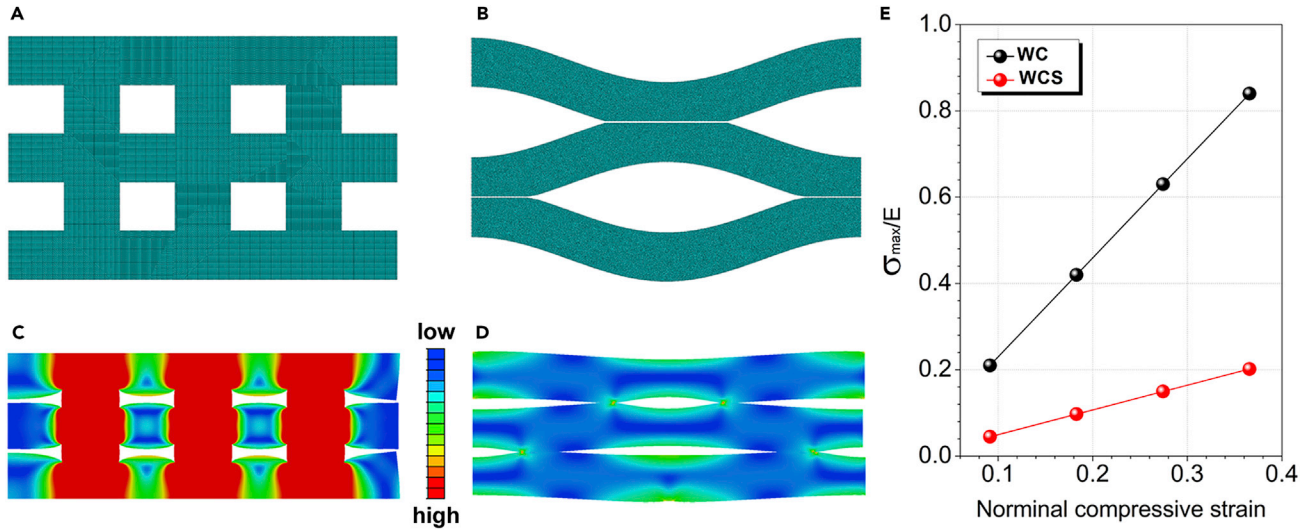

Figure 5. Insights into the Fracture and Anti-fracture Mechanisms of WC and WCS, Respectively

(A) Finite element model for the WC lattice structure.

(B) Finite element model for the lamellar WCS structure.

(C) Distribution of the Mises stress for the WC model at a nominal strain of 36%.

(D) Distribution of the Mises stress for the WCS at a nominal strain of 36%.

(E) Comparison of the evolution of the maximum Mises stress normalized by yield stress for both structures.

foil. A connected light-emitting diode (LED) light becomes brighter when compressing the WCS sensor as a result of an increase in conductivity from the compression (Figures 6C and 6D). This increase is further confirmed by the conductivity test results, which show that the conductivity of the WCS sensor increases significantly from 0.04 to 0.46 S cm^{-1} when ε increases from 0% to 50% and reaches a maximum value of 1.66 S cm^{-1} at a maximum ε of 80% (Figure 6E). The latter is more than 40 times higher than the initial value, demonstrating the high pressure sensitivity of the WCS sensor. Note that the WCS also demonstrates anisotropic electrical properties (0.04 versus 5.49 S cm^{-1}) with an anisotropic factor of 137 (Figure S15). The anisotropic electrical properties can be rationalized by the anisotropic structure: the continuous layer along the *z* direction enables the fast transport of electrons (fast in-plane electron transport), whereas electron transport across multiple stacked layers with abundant pores along the *y* direction is difficult (slow cross-plane electron transport).

Recently, flexible strain sensors with high sensitivity have shown great potential for monitoring human activities, personal health, and other related applications.[44–49] To demonstrate the promising application of the WCS for strain sensing, we attached the WCS sensor chip onto a human finger (inset in Figure 6F). The relative current from the sensor increased significantly as the finger motion progressed from the straight (a) to the bending (b) position (Figure 6F). Repeated square wave signals can be observed during multiple stretch/bend cycles. By controlling the bending of the finger, distinct signals of the current change can be obtained (Figure 6G) as a result of the pressure change during bending. Our results show that the WCS material with excellent mechanical compressibility, fatigue resistance, and high pressure sensitivity can potentially be used as a high-performance strain sensor for human motion or health monitoring. However, the WCS-based strain sensor failed to detect observable electrical responses of human pulses; rather, the activity was much fainter. Further optimization of the structure of WCS is needed to improve the sensitivity to detect such faint movements.

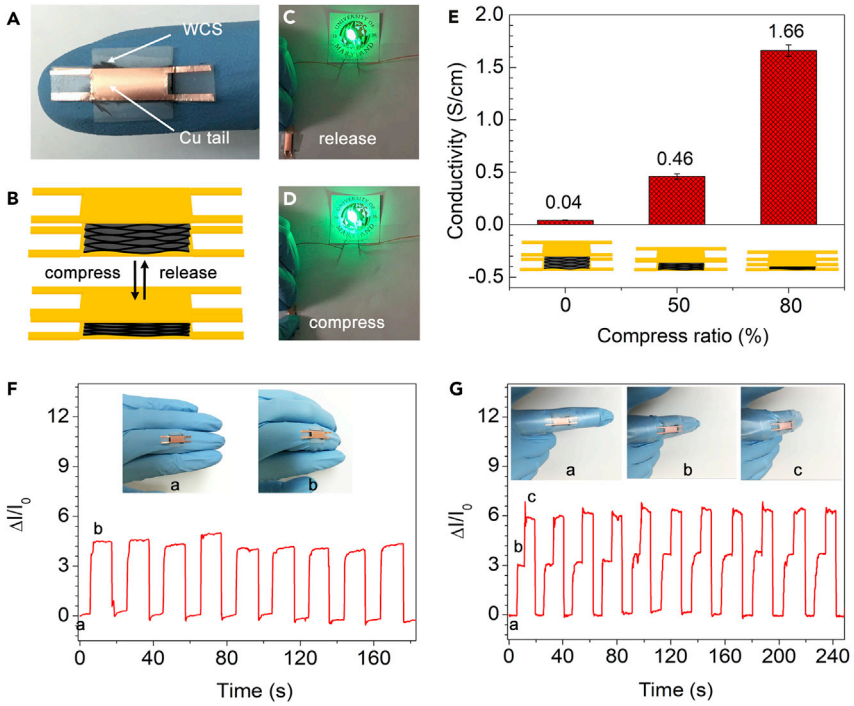

Figure 6. WCS-Based Strain Sensor Performance

(A) Photograph of the WCS strain sensor.

(B) Graphical illustration of the WCS strain sensor under both compression and release conditions.

(C and D) Photographs of the LED light with the WCS strain sensor under release (C) and compression (D) conditions.

(E) Conductivity of the WCS strain sensor with different compression ratios. Error bars indicate standard deviations for three sets of data points.

(F and G) Current changes ($\Delta I/I_0$) under different progressive motions (F, two movements; G, three movements) of the strain sensor on the fingers, shown as insets.

In summary, we have demonstrated a nature-inspired, facile design concept and fabrication process for a highly compressible and anisotropic lamellar carbon sponge directly from natural wood by chemical treatment and carbonization. The WCS has a unique lamellar multi-wave-like layered structure, which leads to a remarkable mechanical compressibility (up to 80% compression strain), fatigue resistance (10,000 stable compression cycles at 50% strain), and pressure sensibility, distinct from the brittle WC. A high-performance strain sensor based on the lamellar WCS material can be achieved, demonstrating a potential application for human motion and health monitoring. This unique lamellar structure, as well as the outstanding mechanical and electrical properties, can potentially enable many future applications, including wearable electronics, rechargeable batteries, supercapacitors, and catalyst supports that are not limited to health monitoring. Moreover, the fabrication process of WCS is facile, sustainable, and scalable, which in turn opens up new opportunities for developing sponge-like functional materials from sustainable natural resources.

EXPERIMENTAL PROCEDURES

Synthesis of Sponge-like Delignified Wood

The wood block was immersed into a boiling mixed aqueous solution (2.5 M NaOH and 0.4 M Na_2SO_3) for 7 hr and then immersed into boiling deionized (DI) water several times for the removal of chemicals. The wood block was then immersed in

boiling H_2O_2 (2.5 M in DI water) for a few hours until the color of the wood turned white. The white wood was then placed in a freezer dryer and dried for 1 day. Sponge-like delignified wood was obtained.

Synthesis of Wood Carbon Sponge

The sponge-like wood was first stabilized in air at 260°C for 6 hr and then carbonized in Ar at 1,000°C for another 6 hr to finally yield the WCS.

All other experimental and setup details, as well the finite element simulations, are provided in the Supplemental Experimental Procedures.

SUPPLEMENTAL INFORMATION

Supplemental Information includes Supplemental Experimental Procedures and 15 figures and can be found with this article online at https://doi.org/10.1016/j.chempr.2017.12.028.

ACKNOWLEDGMENTS

L.H. acknowledges the support of the Maryland NanoCenter and its AIMLab.

AUTHOR CONTRIBUTIONS

L.H., C.C., and J.S. contributed to the idea and experimental design. C.C. and J.S. contributed to the wood treatment and mechanical measurements. Y.L., J.W., D.K., L.X., Yanbin Wang, T.G., Yilin Wang, H.H., W.G., and A G. contributed to the characterization of the materials. C.C. and Y.K. contributed to the 3D illustrations. S.Z. and T.L. contributed to the mechanics modeling and analysis. L.H., J.X., and C.C. contributed to writing the paper. All authors commented on the final manuscript.

DECLARATION OF INTERESTS

The authors declare no competing interests.

Received: September 15, 2017
Revised: December 12, 2017
Accepted: December 28, 2017
Published: March 1, 2018

REFERENCES AND NOTES

1. Sun, H., Xu, Z., and Gao, C. (2013). Multifunctional, ultra-flyweight, synergistically assembled carbon aerogels. Adv. Mater. *25*, 2554–2560.

2. Zhao, Y., Hu, C., Hu, Y., Cheng, H., Shi, G., and Qu, L. (2012). A versatile, ultralight, nitrogen-doped graphene framework. Angew. Chem. Int. Ed. *124*, 11533–11537.

3. Chen, Z., Ren, W., Gao, L., Liu, B., Pei, S., and Cheng, H.M. (2011). Three-dimensional flexible and conductive interconnected graphene networks grown by chemical vapour deposition. Nat. Mater. *10*, 424–428.

4. Wu, Z.Y., Li, C., Liang, H.W., Chen, J.F., and Yu, S.H. (2013). Ultralight, flexible, and fire-resistant carbon nanofiber aerogels from bacterial cellulose. Angew. Chem. Int. Ed. *125*, 2997–3001.

5. Si, Y., Wang, X., Yan, C., Yang, L., Yu, J., and Ding, B. (2016). Ultralight biomass-derived carbonaceous nanofibrous aerogels with superelasticity and high pressure-sensitivity. Adv. Mater. *28*, 9512–9518.

6. Liu, M., Yang, Z., Sun, H., Lai, C., Zhao, X., Peng, H., and Liu, T. (2016). A hybrid carbon aerogel with both aligned and interconnected pores as interlayer for high-performance lithium–sulfur batteries. Nano Res. *9*, 3735–3746.

7. Peng, Q., Li, Y., He, X., Gui, X., Shang, Y., Wang, C., Wang, C., Zhao, W., Du, S., Shi, E., et al. (2014). Graphene nanoribbon aerogels unzipped from carbon nanotube sponges. Adv. Mater. *26*, 3241–3247.

8. Li, C., and Shi, G. (2014). Functional gels based on chemically modified graphenes. Adv. Mater. *26*, 3992–4012.

9. Zhao, X., Yao, W., Gao, W., Chen, H., and Gao, C. (2017). Wet-spun superelastic graphene aerogel millispheres with group effect. Adv. Mater. *29* Published online July 17, 2017. https://doi.org/10.1002/adma.201701482.

10. Gui, X., Wei, J., Wang, K., Cao, A., Zhu, H., Jia, Y., Shu, Q., and Wu, D. (2010). Carbon nanotube sponges. Adv. Mater. *22*, 617–621.

11. Hu, L., Wu, H., Gao, Y., Cao, A., Li, H., McDough, J., Xie, X., Zhou, M., and Cui, Y. (2011). Silicon–carbon nanotube coaxial sponge as Li-ion anodes with high areal capacity. Adv. Energy Mater. *1*, 523–527.

12. Chen, Y., Zhang, H.-B., Yang, Y., Wang, M., Cao, A., and Yu, Z.-Z. (2016). High-performance epoxy nanocomposites reinforced with three-dimensional carbon nanotube sponge for electromagnetic interference shielding. Adv. Funct. Mater. *26*, 447–455.

13. Li, M., Carter, R., Douglas, A., Oakes, L., and Pint, C.L. (2017). Sulfur vapor-infiltrated 3D carbon nanotube foam for binder-free high

areal capacity lithium–sulfur battery composite cathodes. ACS Nano *11*, 4877–4884.

14. Li, M., Carter, R., Cohn, A.P., and Pint, C.L. (2016). Interconnected foams of helical carbon nanofibers grown with ultrahigh yield for high capacity sodium ion battery anodes. Carbon *107*, 109–115.

15. Innocenzi, P., and Brusatin, G. (2001). Fullerene-based organic-inorganic nanocomposites and their applications. Chem. Mater. *13*, 3126–3139.

16. Ge, J., Shi, L.-A., Wang, Y.-C., Zhao, H.-Y., Yao, H.-B., Zhu, Y.-B., Zhang, Y., Zhu, H.-W., Wu, H.-A., and Yu, S.-H. (2017). Joule-heated graphene-wrapped sponge enables fast clean-up of viscous crude-oil spill. Nat. Nanotechnol. *12*, 434–440.

17. Yang, M., Zhao, N., Cui, Y., Gao, W., Zhao, Q., Gao, C., Bai, H., and Xie, T. (2017). Biomimetic architectured graphene aerogel with exceptional strength and resilience. ACS Nano *11*, 6817–6824.

18. Chen, C., Xu, H., Zhou, T., Guo, Z., Chen, L., Yan, M., Mai, L., Hu, P., Cheng, S., Huang, Y., et al. (2016). Integrated intercalation-based and interfacial sodium storage in graphene-wrapped porous $Li_4Ti_5O_{12}$ nanofibers composite aerogel. Adv. Energy Mater. *6*, 1600322.

19. Wang, B., Li, S., Wu, X., Liu, J., and Chen, J. (2016). Biomass chitin-derived honeycomb-like nitrogen-doped carbon/graphene nanosheet networks for applications in efficient oxygen reduction and robust lithium storage. J. Mater. Chem. A *4*, 11789–11799.

20. Liang, H.-W., Wu, Z.-Y., Chen, L.-F., Li, C., and Yu, S.-H. (2015). Bacterial cellulose derived nitrogen-doped carbon nanofiber aerogel: an efficient metal-free oxygen reduction electrocatalyst for zinc-air battery. Nano Energy *11*, 366–376.

21. Xu, X., Zhou, J., Nagaraju, D.H., Jiang, L., Marinov, V.R., Lubineau, G., Alshareef, H.N., and Oh, M. (2015). Flexible, highly graphitized carbon aerogels based on bacterial cellulose/lignin: catalyst-free synthesis and its application in energy storage devices. Adv. Funct. Mater. *25*, 3193–3202.

22. Wu, X.L., Wen, T., Guo, H.L., Yang, S., Wang, X., and Xu, A.W. (2013). Biomass-derived sponge-like carbonaceous hydrogels and aerogels for supercapacitors. ACS Nano *7*, 3589–3597.

23. Li, Y.-Q., Samad, Y.A., Polychronopoulou, K., Alhassan, S.M., and Liao, K. (2014). Carbon aerogel from winter melon for highly efficient and recyclable oils and organic solvents absorption. ACS Sustainable Chem. Eng. *2*, 1492–1497.

24. Dan, L., and Ling, Q. (2017). Super-carbon spring: a biomimetic design. Sci. China Mater. *60*, 186.

25. Gao, H.-L., Zhu, Y.-B., Mao, L.-B., Wang, F.-C., Luo, X.-S., Liu, Y.-Y., Lu, Y., Pan, Z., Ge, J., Shen, W., et al. (2016). Super-elastic and fatigue resistant carbon material with lamellar multi-arch microstructure. Nat. Commun. *7*, 12920.

26. Chen, C., Li, Y., Song, J., Yang, Z., Kuang, Y., Hitz, E., Jia, C., Gong, A., Jiang, F., Zhu, J.Y., et al. (2017). Highly flexible and efficient solar steam generation device. Adv. Mater. *29*, 1701756.

27. Song, J., Chen, C., Wang, C., Kuang, Y., Li, Y., Jiang, F., Li, Y., Hitz, E., Zhang, Y., Liu, B., et al. (2017). Super flexible wood. ACS Appl. Mater. Interfaces *9*, 23520–23527.

28. Ding, J., Wang, H., Li, Z., Kohandehghan, A., Cui, K., Xu, Z., Zahiri, B., Tan, X., Lotfabad, E.M., Olsen, B.C., et al. (2013). Carbon nanosheet frameworks derived from peat moss as high performance sodium ion battery anodes. ACS Nano *7*, 11004–11015.

29. Chen, C., Wang, Z., Zhang, B., Miao, L., Cai, J., Peng, L., Huang, Y., Jiang, J., Huang, Y., Zhang, L., et al. (2017). Nitrogen-rich hard carbon as a highly durable anode for high-power potassium-ion batteries. Energy Storage Mater. *8*, 161–168.

30. Chen, W., Chen, C., Xiong, X., Hu, P., Hao, Z., and Huang, Y. (2017). Coordination of surface-induced reaction and intercalation: toward a high-performance carbon anode for sodium-ion batteries. Adv. Sci. *4*, 1600500.

31. Xu, D., Chen, C., Xie, J., Zhang, B., Miao, L., Cai, J., Huang, Y., and Zhang, L. (2016). A hierarchical N/S-codoped carbon anode fabricated facilely from cellulose/polyaniline microspheres for high-performance sodium-ion batteries. Adv. Energy Mater. *6*, 1501929.

32. Chen, C., Zhang, Y., Li, Y., Dai, J., Song, J., Gong, Y., Kierzewski, I., Xie, J., and Hu, L. (2017). All-wood, low tortuosity, aqueous, biodegradable supercapacitors with ultra-high capacitance. Energy Environ. Sci. *10*, 538–545.

33. Zhang, Y., Luo, W., Wang, C., Li, Y., Chen, C., Song, J., Dai, J., Hitz, E.M., Xu, S., Yang, C., et al. (2017). High-capacity, low-tortuosity, and channel-guided lithium metal anode. Proc. Natl. Acad. Sci. USA *114*, 3584–3589.

34. Wu, Y., Yi, N., Huang, L., Zhang, T., Fang, S., Chang, H., Li, N., Oh, J., Lee, J.A., Kozlov, M., et al. (2015). Three-dimensionally bonded spongy graphene material with super compressive elasticity and near-zero Poisson's ratio. Nat. Commun. *6*, 6141.

35. Cao, A., Dickrell, P.L., Sawyer, W.G., Ghasemi-Nejhad, M.N., and Ajayan, P.M. (2005). Super-compressible foamlike carbon nanotube films. Science *310*, 1307–1310.

36. Kim, K.H., Oh, Y., and Islam, M. (2012). Graphene coating makes carbon nanotube aerogels superelastic and resistant to fatigue. Nat. Nanotechnol. *7*, 562–566.

37. Si, Y., Yu, J., Tang, X., Ge, J., and Ding, B. (2014). Ultralight nanofibre-assembled cellular aerogels with superelasticity and multifunctionality. Nat. Commun. *5*, 5802.

38. Si, Y., Fu, Q., Wang, X., Zhu, J., Yu, J., Sun, G., and Ding, B. (2015). Superelastic and superhydrophobic nanofiber-assembled cellular aerogels for effective separation of oil/water emulsions. ACS Nano *9*, 3791–3799.

39. Li, Y., Chen, J., Huang, L., Li, C., Hong, J.D., and Shi, G. (2014). Highly compressible macroporous graphene monoliths via an improved hydrothermal process. Adv. Mater. *26*, 4789–4793.

40. Qiu, L., Liu, J.Z., Chang, S.L., Wu, Y., and Li, D. (2012). Biomimetic superelastic graphene-based cellular monoliths. Nat. Commun. *3*, 1241.

41. Gui, X., Zeng, Z., Zhu, Y., Li, H., Lin, Z., Gan, Q., Xiang, R., Cao, A., and Tang, Z. (2014). Three-dimensional carbon nanotube sponge-array architectures with high energy dissipation. Adv. Mater. *26*, 1248–1253.

42. Hu, H., Zhao, Z., Wan, W., Gogotsi, Y., and Qiu, J. (2013). Ultralight and highly compressible graphene aerogels. Adv. Mater. *25*, 2219–2223.

43. Xue, Y., Liu, J., Chen, H., Wang, R., Li, D., Qu, J., and Dai, L. (2012). Nitrogen-doped graphene foams as metal-free counter electrodes in high-performance dye-sensitized solar cells. Angew. Chem. Int. Ed. *51*, 12124–12127.

44. Wang, C., Li, X., Gao, E., Jian, M., Xia, K., Wang, Q., Xu, Z., Ren, T., and Zhang, Y. (2016). Carbonized silk fabric for ultrastretchable, highly sensitive, and wearable strain sensors. Adv. Mater. *28*, 6640–6648.

45. Yu, X., Pan, J., Zhang, J., Sun, H., He, S., Qiu, L., Lou, H., Sun, X., and Peng, H. (2017). A coaxial triboelectric nanogenerator fiber for energy harvesting and sensing under deformation. J. Mater. Chem. A *5*, 6032–6037.

46. Zhong, J., Zhong, Q., Hu, Q., Wu, N., Li, W., Wang, B., Hu, B., and Zhou, J. (2015). Stretchable self-powered fiber-based strain sensor. Adv. Funct. Mater. *25*, 1798–1803.

47. Lu, X., Zhang, Z., Sun, X., Chen, P., Zhang, J., Guo, H., Shao, Z., and Peng, H. (2016). Flexible and stretchable chromatic fibers with high sensing reversibility. Chem. Sci. *7*, 5113–5117.

48. Jian, M., Xia, K., Wang, Q., Yin, Z., Wang, H., Wang, C., Xie, H., Zhang, M., and Zhang, Y. (2017). Flexible and highly sensitive pressure sensors based on bionic hierarchical structures. Adv. Funct. Mater. *27*, 1606066.

49. Liu, Q., Chen, J., Li, Y., and Shi, G. (2016). High-performance strain sensors with fish-scale-like graphene-sensing layers for full-range detection of human motions. ACS Nano *10*, 7901–7906.

Chem, Volume *4*

Supplemental Information

Scalable and Sustainable Approach toward Highly Compressible, Anisotropic, Lamellar Carbon Sponge

Chaoji Chen, Jianwei Song, Shuze Zhu, Yiju Li, Yudi Kuang, Jiayu Wan, Dylan Kirsch, Lisha Xu, Yanbin Wang, Tingting Gao, Yilin Wang, Hao Huang, Wentao Gan, Amy Gong, Teng Li, Jia Xie, and Liangbing Hu

Supplementary Information

Supplemental Figures

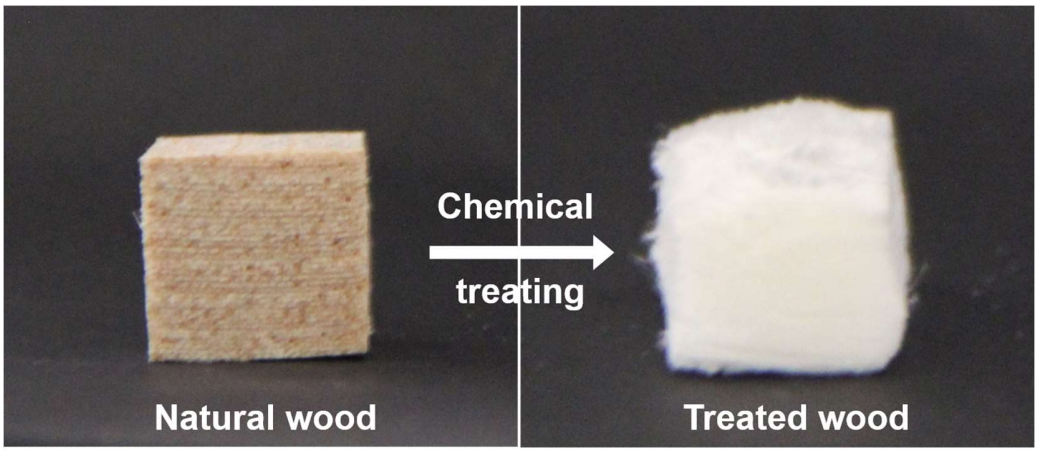

Figure S1. Photo Images of the Natural Wood and Treated Wood (Wood Sponge). It shows that the yellow natural wood becomes totally white after chemical treating due to the removal of lignin.

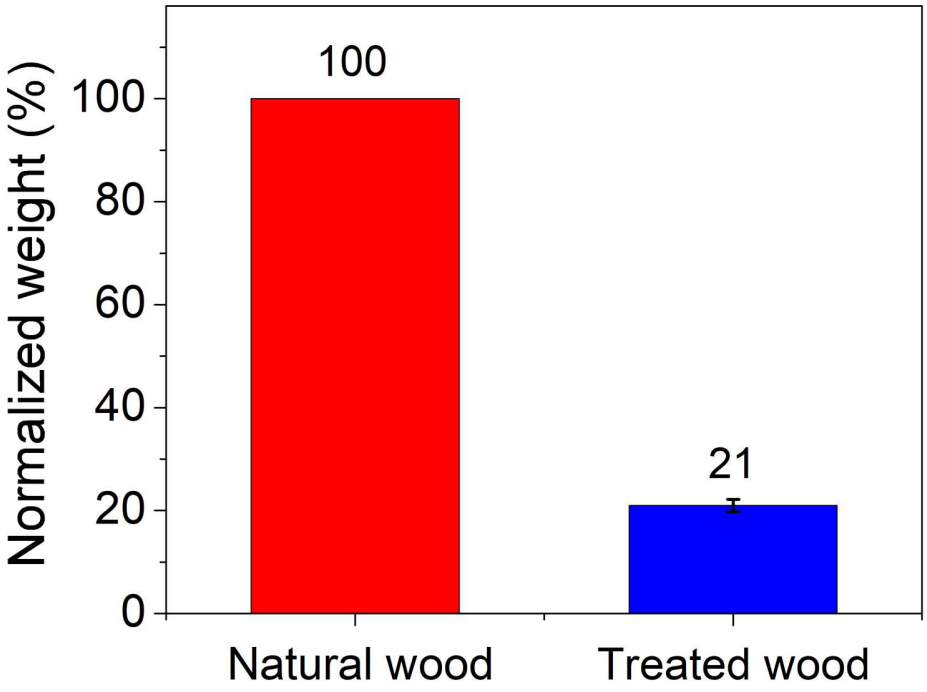

Figure S2. Weight Loss of the Wood Samples before and after Chemical Treatment. Error bars indicate standard deviations for 3 sets of data points.

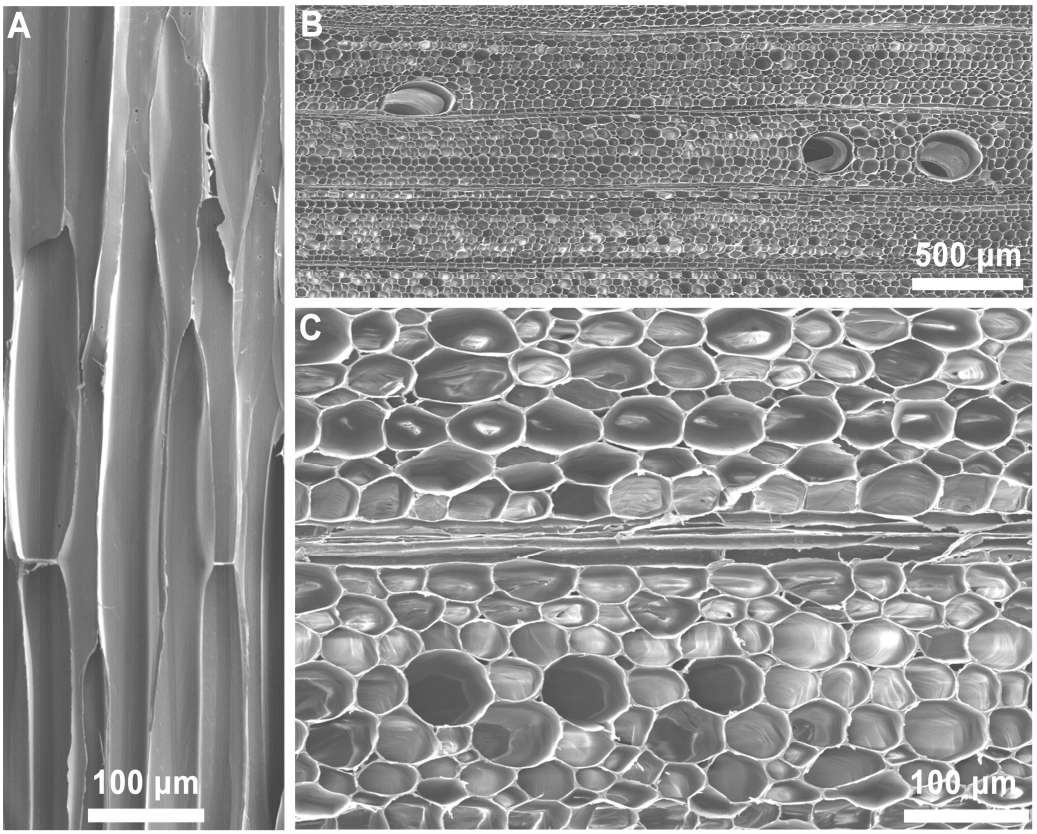

Figure S3. SEM Images of the Natural Balsa Wood. (A) Cross-section-view image, showing the channels along the growth direction. (B,C) Top-view images, showing the lattice-like structure of the natural wood with numerous channels.

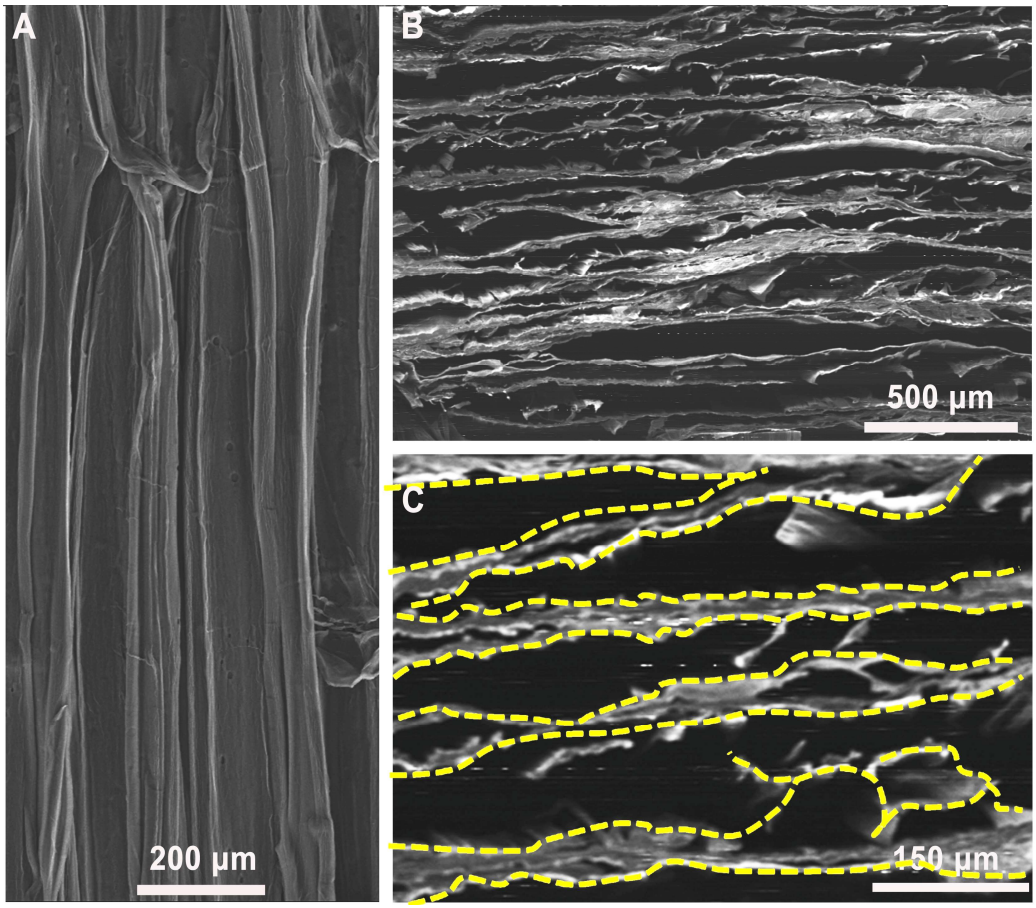

Figure S4. SEM Images of the Compressible Wood Sponge. (A) Cross-section-view image, showing that the channels along the growth direction become inconspicuous due to the chemical treating. (B,C) Top-view images, showing the lamellar structure comprised of numerous stacking curved layers.

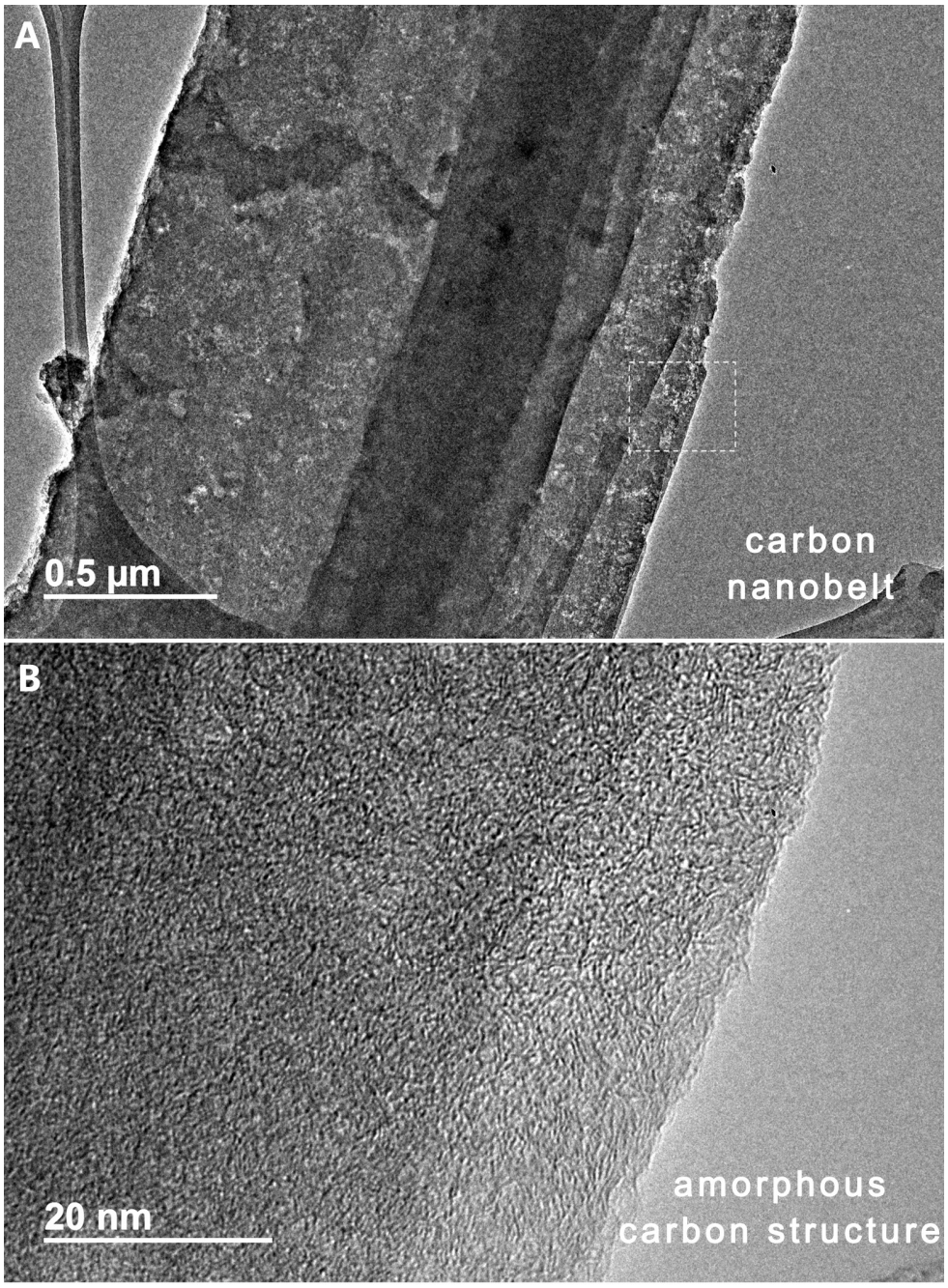

Figure S5. TEM and HR-TEM Images of the Wood Carbon Sponge. (A) TEM image. (B) HR-TEM image. Many disordered domains can be observed in the HR-TEM image, suggesting the wood carbon sponge has amorphous features.

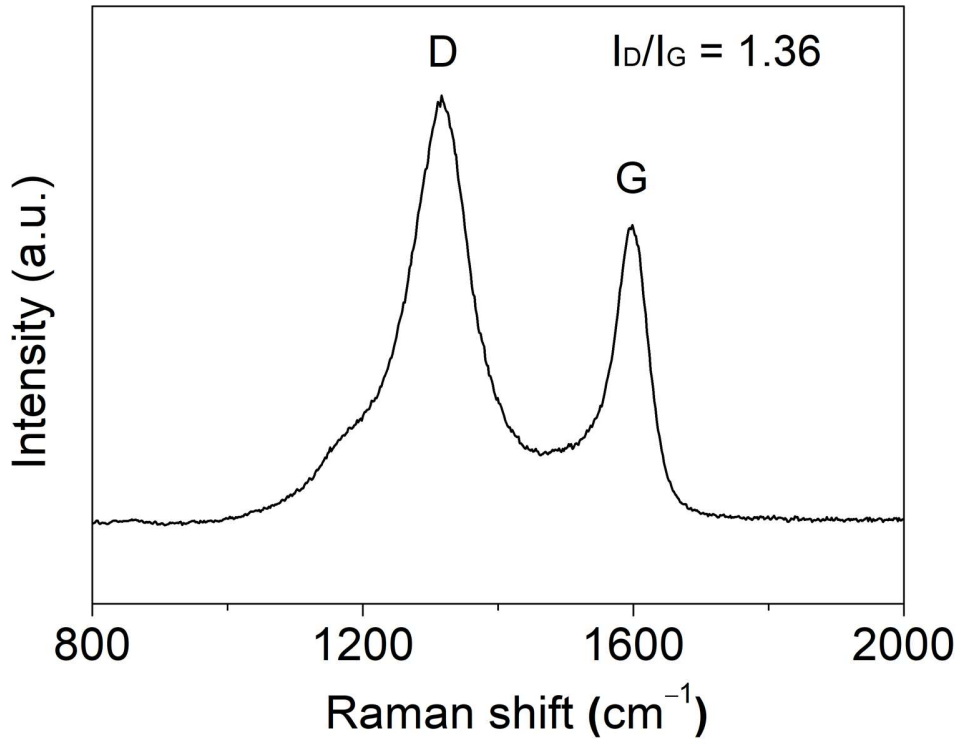

Figure S6. Raman Spectrum of the Wood Carbon Sponge. The obvious D and G peaks with a I_D/I_G value of 1.36 indicates the amorphous features of the wood carbon sponge.

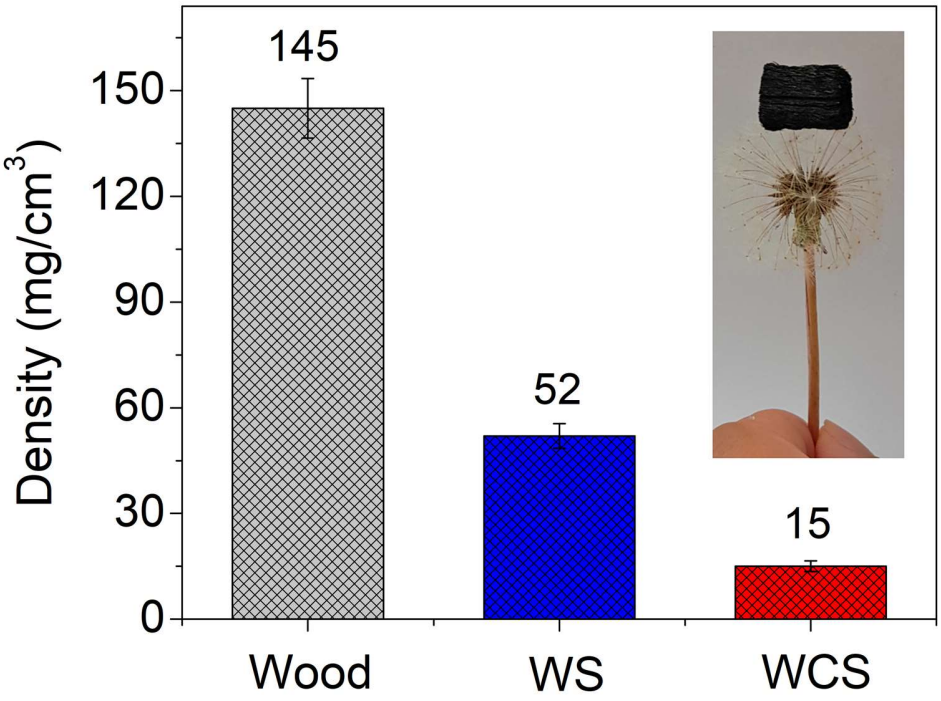

Figure S7. Density Evolutions from Natural Wood, to Wood Sponge (WS), and Wood Carbon Sponge (WCS). Inset shows the lightweight feature of the wood carbon sponge. Error bars indicate standard deviations for 3 sets of data points.

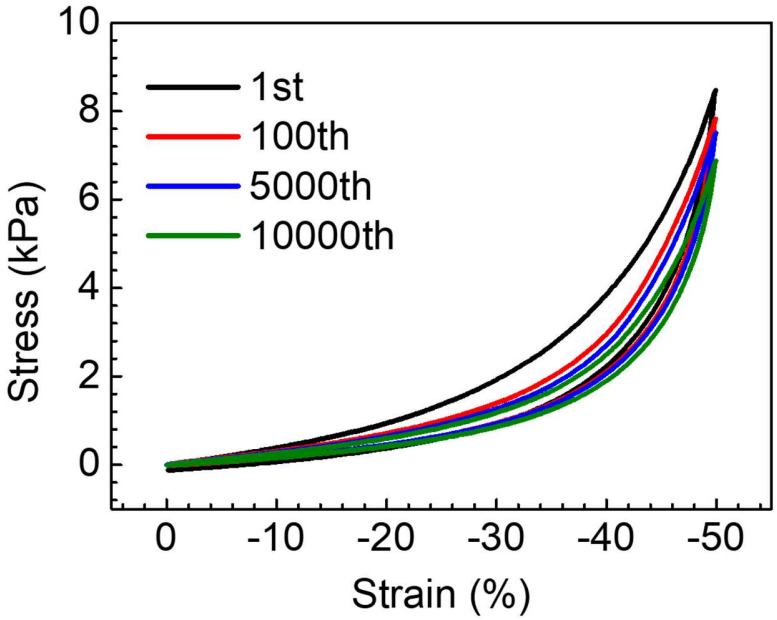

Figure S8. Stress-Strain Curves of the WCS Obtained in Selected Cycles of 1st, 100th, 5000th, and 10000th.

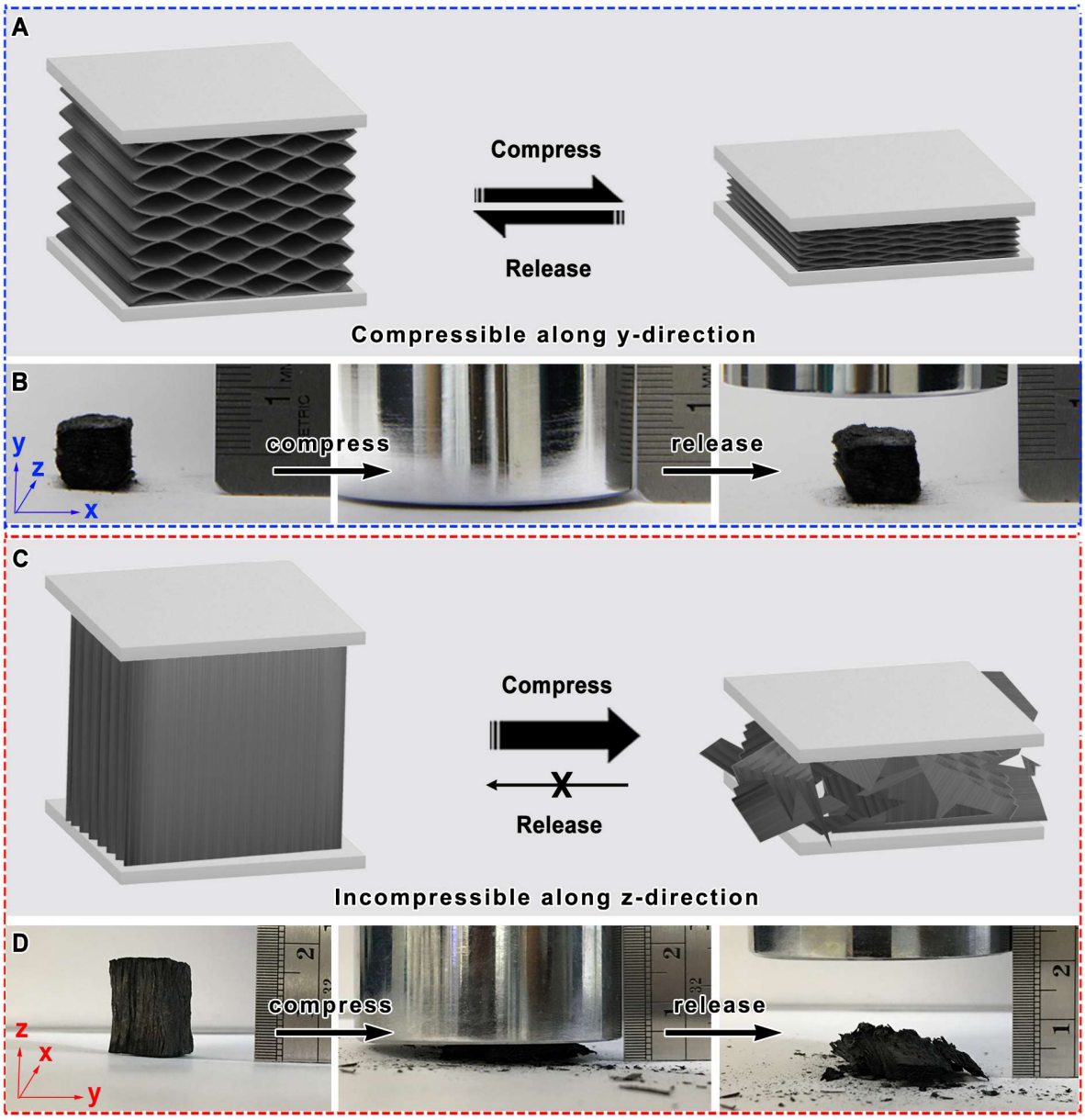

Figure S9. Anisotropic Mechanical Properties of the Wood Carbon Sponge. (A) Graphical illustration and (B) digital images of the compressible property of the wood carbon sponge along y-direction. (C) Graphical illustration and (D) digital images of the incompressible property of the wood carbon sponge along z-direction.

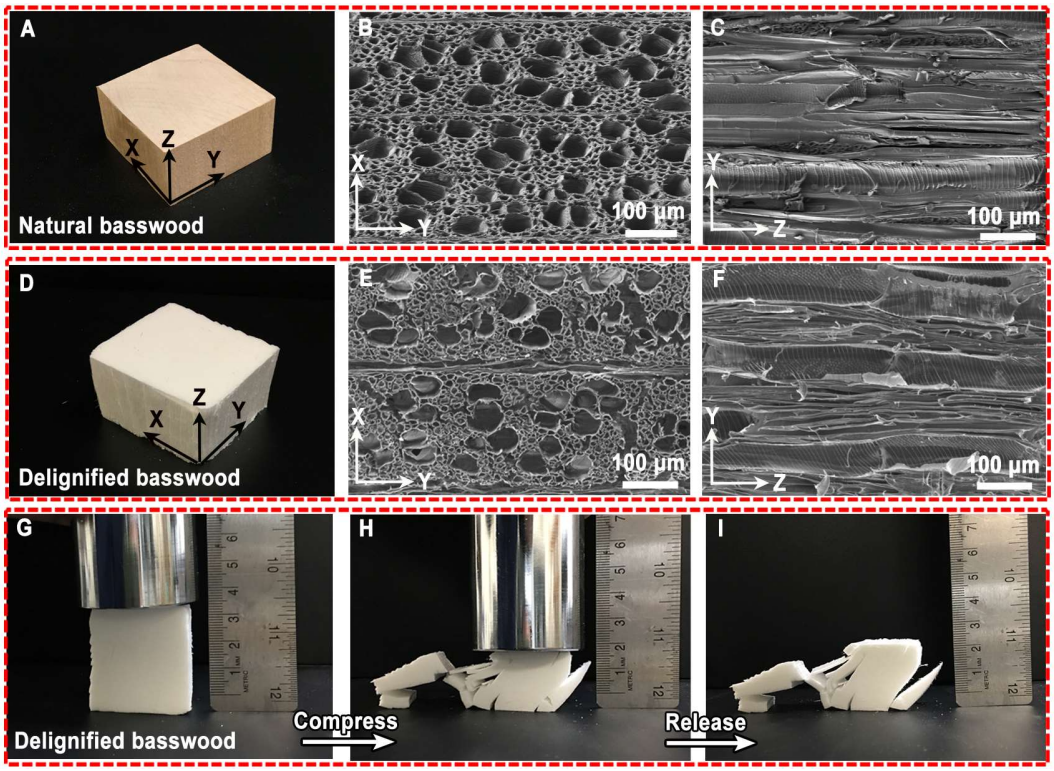

Figure S10. Structural Characterization of the Natural Basswood and Delignified Basswood. (A) Digital image of the natural wood. (B,C) SEM images of the natural basswood: (B) cross-sectional image showing the wood lumen structure (in XY plane); (C) longitudinal image showing the lumina along the growth direction (in YZ plane). (d) Photo image of the white basswood. (E,F) SEM images of the wood aerogel: (E) cross-sectional SEM image showing the structure in XY plane; (F) longitudinal SEM image showing the lumina along the growth direction (in YZ plane). (G-I) Photo images of the white basswood before compressing (G), under compression (H) and after recovery (I), respectively.

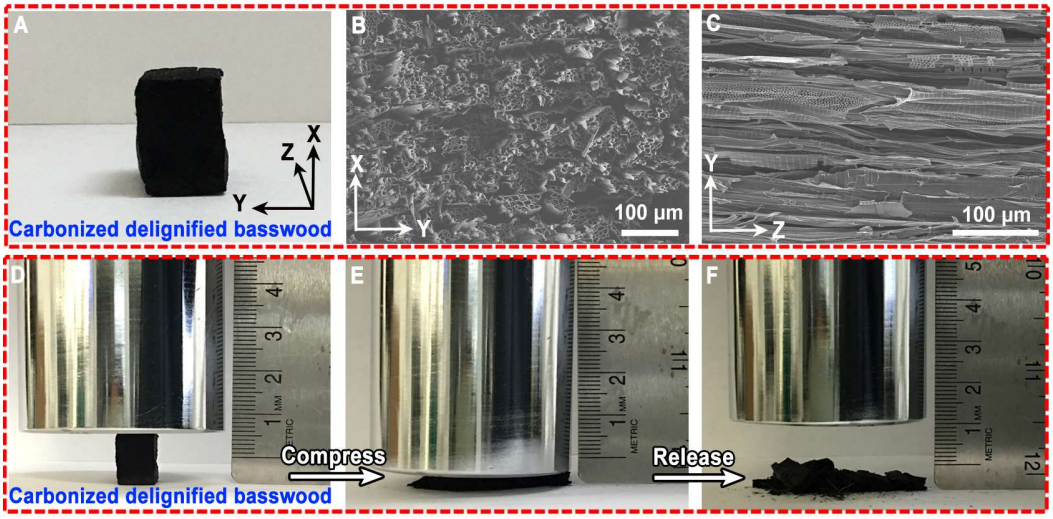

Figure S11. Structural Characterization of the Carbonized Delignified Basswood. (A) Digital image of the carbonized delignified basswood. (B,C) SEM images of the carbonized delignified basswood: (B) cross-sectional image showing the wood lumen structure (in XY plane); (C) longitudinal image showing the lumina along the growth direction (in YZ plane). (D-F) Digital images of the carbonized delignified basswood before compression (D), under compression (E) and after recovery (F), respectively.

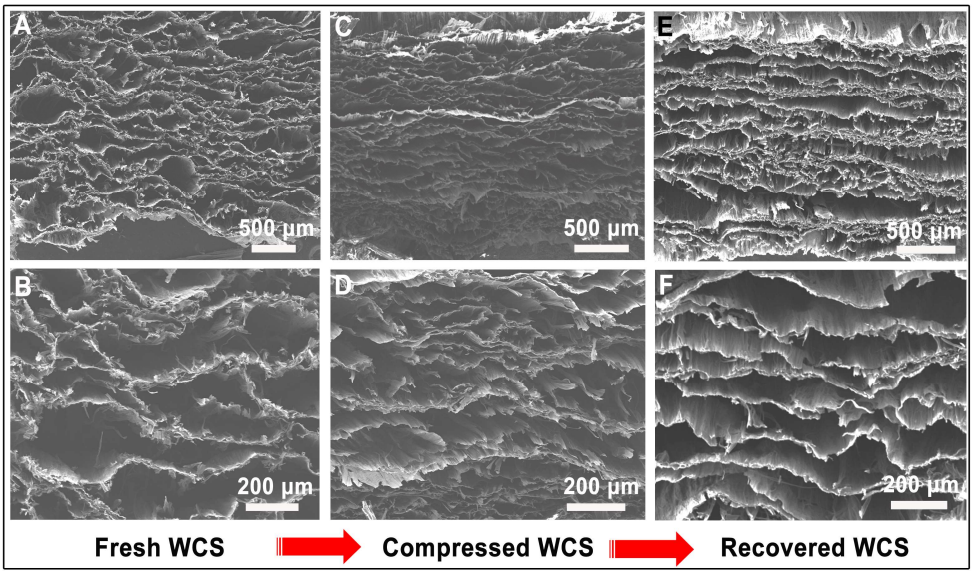

Figure S12. *Ex-situ* SEM Observations of the Wood Carbon Sponge. (A,B) Before compression. (C,D) During compression. (E,F) After releasing. Due to the arched layered structure, stress can be easily released by the small local bending of the arched layers, resulting in an excellent compressibility.

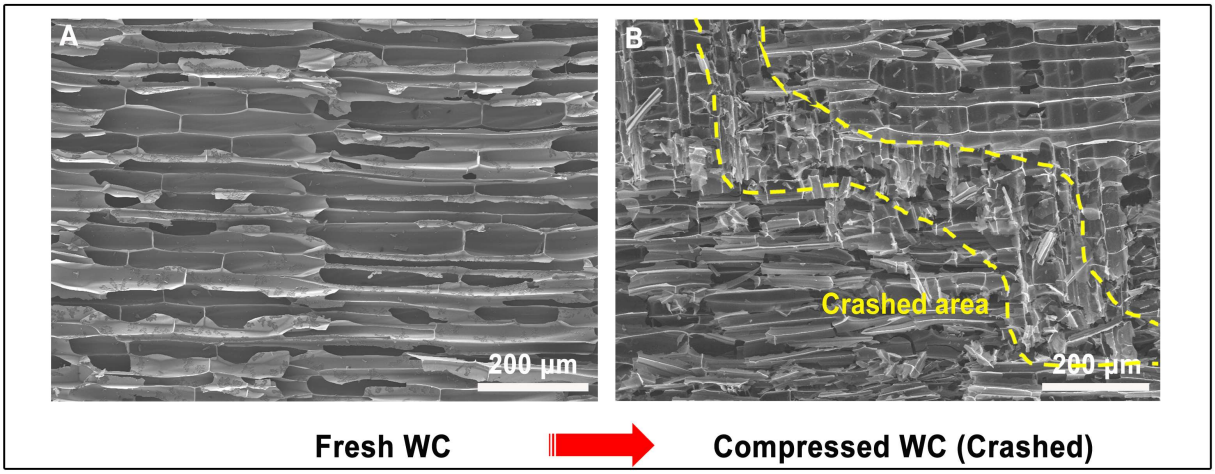

Figure S13. *Ex-situ* SEM Observations of the Wood Carbon. (A) Before compression. (B) After compression. The results show that the wood carbon, with a lattice-like structure, is easy to be crushed due to the stress concentrations at the cell merge points.

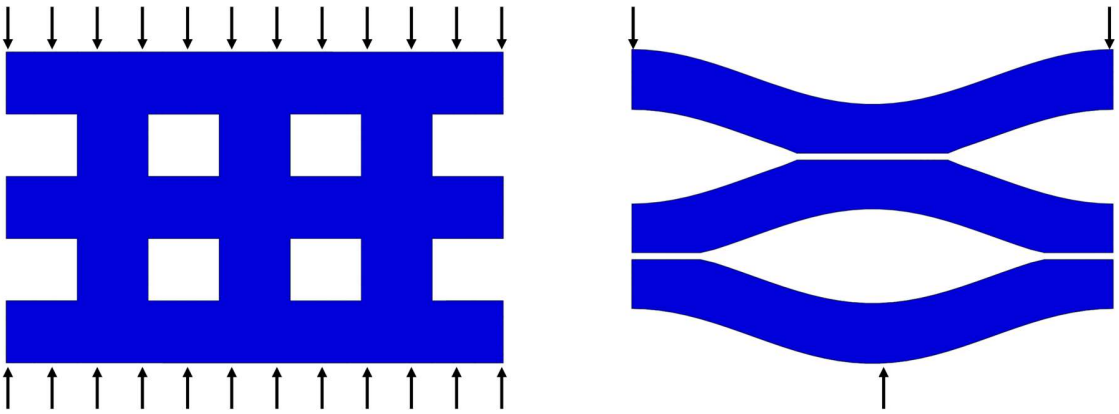

Figure S14. Finite Element Simulation Models of WC (Left) and WCS (Right).

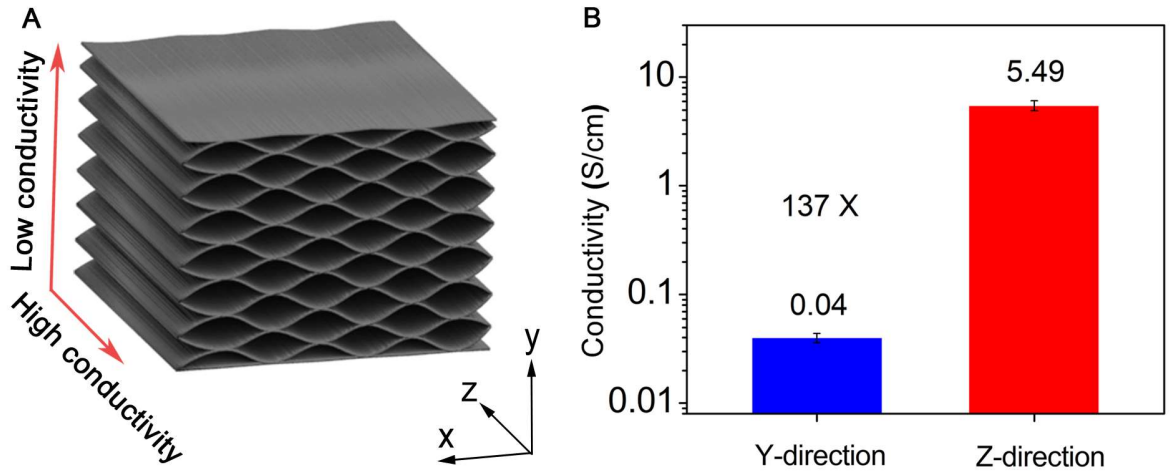

Figure S15. Anisotropic Electrical Properties of WCS. (A) Graphical illustration of the anisotropic structure and electrical conductivity of the wood carbon sponge. (B) Electrical conductivities of the wood carbon sponge along y- and z-directions with an anisotropic factor of ~137. Error bars indicate standard deviations for 3 sets of data points.

Supplemental Experimental Procedures

Characterizations:

The morphology and structure of materials were characterized by scanning electron microscopy (SEM, Hitachi SU-70), transmission electron microscopy (TEM, JEOL 2100F field-emission TEM) and X-ray diffraction (XRD, Rigaku Ultima III using Cu K α radiation (λ = 1.5406 Å)). Raman spectrum was collected on a commercial micro Raman spectrometer (Labram Aramis model manfuctured by Horiba Jobin Yvon). FT-IR spectrum was measured on a Thermo Nicolet NEXUS 670 FTIR. Compositional analysis was carried out on a high-performance liquid chromatography (HPLC) (Ultimate 3000, Thermo Scientific, USA). The mechanical compression test was performed on a universal testing machine (SHIMADZU AGS-X) with loading capacity from 0.01 to 170 N at a constant loading and unloading speed of 2 mm/min. For fatigue measurements at 50% strain for 10,000 cycles, the interval compression cycles were conducted by using a Dynamic Mechanical Analyzer (RSA 3, TA instruments) at 1 Hz. The electrical signals of the strain sensors were recorded at a Keithley 2400 digital meter at a constant voltage of 0.1 V.

Finite Element Simulations:

The finite element simulation is carried out using commercial code ABAQUS 6.10. The CPS4R, a 4-node bilinear plane stress quadrilateral element is used to mesh both the WCS model and the WC model. For the purpose of comparison, we keep the thickness of the channel walls in the WC structure model and the curved layers in the WCS structure model roughly the same, while strictly maintaining the same height (21.875 length unit), the same length (35 length unit), and same width (35 length unit) of the entire model. The mathematic description of the curved shape is a sinusoidal function, but it adopts a straight-line shape at the contact region between layers. Then an initial separation (0.5 length unit) between the curved layers is introduced in the WCS structure model for defining the contact between surfaces. Such a contact is modeled by using hard contact as the normal behavior and frictionless resistance as the tangential behavior. Displacement loading is applied as shown in **Figure S14**. The elastic properties are set as the following - Young's Modulus: 10 GPa, Poisson's ratio: 0.3.